In silico identification of potential allosteric inhibitors of the SARS-CoV-2 Helicase

Adekunle Babajide. Rowaiye[1], Olukemi Adejoke Onuh[1], Titilayo Mercy Asala[1], Amoge Chidinma Ogu[1], Doofan Bur[1], Ezinne Janefrances Nwankwo[1], Uchenna Maryrose Orji[1], Zainab Rafindadi Ibrahim[1], Jamila Hamza[1], Adaku Lizzy Ugorji[1]*

[1]Department of Medical Biotechnology, National Biotechnology Development Agency, Lugbe, Abuja, Nigeria.

***Corresponding author.**

E-mail address: adekunlerowaiye@gmail.com (Adekunle B. Rowaiye).

ABSTRACT

The COVID-19 pandemic ravages the globe causing unprecedented health and economic challenges. As the world prospects for a cure, scientists are looking critically at strategic protein targets within the SARS-CoV-2 that have therapeutic significance. One of such targets is the Helicase which is an enzyme that affects all aspects of SARS-CoV-2 RNA metabolism. The aim of this study is to identify small molecules from natural products that have strong binding affinity with and inhibitory activity against an allosteric site (Pocket 26) of SARS-CoV-2 Helicase. Pyrx was used for the *in silico* molecular docking simulations of SARS-CoV-2 Helicase (QHD43415-12.pdb) against a library of small molecules obtained from edible African

plants. Triphenylmethane which had a docking score of -7.4 kcal/mol was chosen as a reference molecule. Virtual screening for oral bioavailability was done based on the molecular descriptors of the compounds as provided by Pubchem. SwissADME, pkCSM, and Molinspiration were used for further screening for molar refractivity, saturation, promiscuity, pharmacokinetic properties, and bioactivity respectively. The Galaxy webserver which uses the GROMACS software was used for the molecular dynamic simulation and analyses. The lead compounds are Gibberellin A12, A20 and A51 obtained from Green peas and the Okra plant. Gibberellin A20 and A51 performed better than the standard. Gibberellin A51 is predicted to show the greatest inhibitory activity against SARS-CoV-2 Helicase. It is recommended that the inhibitory activities of the lead compounds be further investigated.

KEYWORDS: COVID-19; SARS-CoV-2; Helicase; Gibberellin; Molecular Dynamic Simulation.

INTRODUCTION

The Coronavirus disease 2019 (COVID-19) pandemic is an unprecedented global public health challenge which currently affects 213 countries and territories around the world. As of April 15, 2020, the World Health Organization (WHO) has reported about 2,000,000 global cases of COVID-19 with 128,886 deaths (1). COVID-19 is an infectious disease caused a 2019-novel coronavirus (nCoV, SARS-CoV-2) which spreads through droplets of saliva or discharge from the nose when an infected person coughs or sneezes. The symptoms are non-specific. The disease can be asymptomatic but can present a range of symptoms such as fever, dry cough, fatigue, body pains, sore throat, diarrhea, headache and loss of smell or taste. In severe cases, patients suffer pneumonia, severe acute respiratory syndrome, multi-organ and death (2).

The WHO is yet to approve any vaccine or antiviral drug for the prevention or treatment of coronavirus infections. However, some existing broad-spectrum antiviral drugs have been adopted for the treatment of CoV-associated pathologies. Most treatment strategies focus on symptomatic management and supportive therapy only (3, 4).

Before gaining public health importance in 2002, Coronaviruses (CoVs) have been known to infect a wide variety of mammals and birds causing respiratory and enteric diseases. They are classified in four different genera namely the alpha-, beta-, gamma- and delta-CoVs. The CoV genome is susceptible to frequent mutations and recombination which can give rise to new strains of varying virulence (5). There are seven strains of human CoVs, which include 229E, NL63, OC43, HKU1, Middle East respiratory syndrome (MERS)-CoV, severe acute respiratory syndrome (SARS)-CoV, and 2019-novel coronavirus (nCoV). Their major predilection site is the upper and lower respiratory tract causing symptoms such as common cold, pneumonia, bronchiolitis, rhinitis, pharyngitis, and sinusitis (6, 7). CoVs were known to cause milder disease

but the previous epidemics of high-morbidity caused by the SARS-CoV in 2003 and MERS-CoV in 2012, highlighted their adaptive potential to the changing environmental conditions and as such they are now classified as “emerging viruses” (8).

CoVs are enveloped, positive-sense, single-stranded RNA (+ ssRNA) viruses with genome size with a genome size ranging between 26.2 and 31.7 kb (9). They are named after their crown-like appearance in electron micrographs, which is caused by the club-shaped peplomers that radiate outwards from the viral envelope (10, 11).

SARS-CoV-2 belongs to the β genus and contains Structural and Non-Structural Proteins (NSPs). The structural proteins include the Spike (S), Envelop (E), Membrane (M) and Nucleocapsid (N) proteins (12). The spike surface glycoprotein promotes host attachment, and virus-cell membrane fusion during virus infection. It is a major target of neutralizing antibodies (13, 14).

One of the NSPs which is the Helicase enzyme is a motor protein that utilizes the energy derived from nucleotide hydrolysis to unwind double-stranded nucleic acids into two single-stranded nucleic acids along the 5’ – 3’ direction (15, 16, 17). Helicases are not only involved in the unwinding of nucleic acids during recombination, replication, and repair. Recent studies have shown that helicases are also involved in other biological processes such as transcription, mRNA splicing, mRNA export, translation, RNA stability, packaging of nucleic acids into virions and mitochondrial gene expression (18, 19, 20, 21,10). Their validity as antiviral drug targets were recently confirmed when compounds that inhibit a helicase encoded by Herpes Simplex Virus (HSV) were shown to block viral replication and disease progression in animal models (9, 22).

The SARS-CoV-2 Helicase has 596 amino acids and adopts a triangular pyramid shape comprising of 5 domains, just like SARS-CoV and MERS Helicases (23, 24). The domains

include two RecA-like domains (1A and 2A) at the C-terminal Helicase core, the beta-barrel domain (1B), the N-terminal Zinc Binding Domain (ZBD) and the Stalk domain which connects the ZBD and 1B. (23, 24, 25).

The active site of SARS-CoV-2 Helicase has 6 key residues (Lys288, Ser289, Asp374, Glu375, Gln404 and Arg567) which are involved in NTP hydrolysis (23, 24). These residues are found in the cleft at the base between the 1A and 2A domains (24). Thus, small-molecules capable of inhibiting NTPase activity by disrupting ATP binding are ideal strategy to develop helicase inhibitors (23).

However, the SARS-CoV-2 Helicase is an allosteric enzyme suggesting that it can be inhibited through competitive and non-competitive agents at several binding pockets (26). As predicted by *Fpocket* this project focuses on an allosteric site on pocket 26 in which the hydrocarbon, Triphenylmethane a basic structural component of synthetic dyes is known to be an inhibitor (27). Pocket 26 contains the residues VAL6, ARG21, ARG22, PRO23, PHE24, ARG129, LEU132, PHE133, GLU136, PRO234 and LEU235. However, other allosteric sites abound, one of which is pocket 25 which the antiviral drug, Darunavir inhibits (28).

Several small molecules have been shown or predicted to be helicase inhibitors. They include natural products especially flavonoids such as hesperidin, rutin, quercetagetin, xanthones, triptexanthoside D and phyllaemblinol (29). The flavonoids, scutellarein and myricetin are potent inhibitors of the SARS-CoV helicase *in vitro.* They do this by affecting the ATPase activity and not the unwinding activity (30). Other natural products which include Bananin, eubananin, iodobananin, and vanillinbananin, have been shown to be effective inhibitors of the ATPase activity of the SARS-CoV Helicase (31).

Synthetic chemical inhibitors of the enzymatic activities of SARS Helicase include (E)-3-(furan-2-yl)-N-(4-sulfamoylphenyl) acrylamide, 7-ethyl-8-mercapto-3-methyl-3,7-dihydro-1H-purine-2,6-dione and SSYA10-001, a 1,2,4 triazole (32, 33, 34). In terms of drug repurposing, anti-HIV-1 (saquinavir), anti-bacterials (lymecycline, cefsulodine and rolitetracycline), anti-fungal (itraconazole), diuretic (canrenoic) and anti-coagulant (dabigatran) have been predicted to be helicase inhibitors with strong binding affinities (29).

Currently, there are no antiviral drugs specific for SARS-CoV-2 infection (29). Computational drug discovery provides a fast approach for discovery, design and development of therapeutic small-molecule inhibitors against important viral proteins (35, 23). SARS-CoV-2 Helicase (nsp13), similar to that of SARS-CoV, is one of the most important targets for the development of small-molecule inhibitors due to its distinct biological function, active site and highly conserved sequences among coronaviruses (23, 24, 29).

MATERIALS AND METHODS

Preparation, analysis and validation of target protein structure

The 3D structure of SARS-CoV-2 helicase in Protein Data Bank (pdb) format (ID: QHD43415_12.pdb) was obtained from I-TASSER online server with an estimated Template Modelling (TM) score of 0.99. This webserver is used for prediction of protein structure and function (36). The architecture of the target protein was revealed by the Volume, Area, Dihedral Angle Reporter (VADAR 1.8) webserver. The target was analysed using the Ramanchandran plot obtained from the MolProbity web server (37).

Ligand preparation

1,048 compounds obtained from natural products such as spices, edible fruits and vegetables were downloaded from *PubChem* (38). All compounds in the library were pre-screened with the Lipinski's Rule of Five and Veber's Rule, i.e. molecular weight ≤ 500, hydrogen bond donor (HBD) ≤ 5, hydrogen bond acceptor (HBA) ≤ 10, logP ≤ 5, polar surface area (PSA) ≤ 140, and rotatable bonds ≤ 10 (39). Their 3D structures and that of the reference compound, Triphenylmethane (PubChem CID 10614) were downloaded from *PubChem* in sdf format (38).

Molecular docking and virtual screening

1,048 Lipinski and Veber rule-compliant compounds and the reference compound were uploaded to the virtual screening software, *PyRx* (Python Prescription) 0.8 using the *Open Babel* plug-in tool (40). The ligands were subjected to energy minimization and then transformed from structure-data file (sdf) to Protein Data Bank, Partial Charge, & Atom Type (pdbqt) format in preparation for molecular docking. All ligands and the reference molecule were docked against the target protein, SARS-CoV-2 Helicase using *AutoDock Vina* plug-in tool in *Pyrx* (41). The grid parameters for docking with the target protein were set at: Centre X = 79.7763, Y = 79.8336, Z = 79.8336 and Dimensions (Angstrom): X = 89.9405, Y = 65.6233, Z = 77.6795. For stable conformation, Universal Force Field (UFF) and the conjugate gradient descent was used as the energy minimization parameter and optimization algorithm respectively.

The docking results were exported in comma-separated values (csv) format to Microsoft Excel for filtering. Only ligands that had binding affinity scores less than that of the reference compound, Triphenylmethane (-7.4 kcal/mol) were selected. The prediction of pharmacokinetic properties, molar refractivity and bioactivity of all ligands were performed using *pkCSM, SwissADME* and *Molinspiration,* respectively (42, 43, 44).

Analysis of the binding site

Docked poses of all the front-runner compounds were superimposed with the target protein using the *Pymol* software (45). The resultant structures were evaluated using the *Protein-Ligand Interaction Profiler* webserver. (46). All binding pockets of SARS-CoV-2 Helicase were analysed with *Fpocket* online server (47). The three-dimensional depictions of the best docked complexes were analysed using hydrogen bonds, salt bridges and other protein-ligand interactions (46).

Molecular Dynamics Simulations (MDS) and Analyses

The Galaxy (versions 2019.1 and 2019.1.4) supercomputing server which uses the GROMACS software was used to perform the MDS of The Apo and Holo structures of SARS-CoV-2 Helicase (48). The *LigParGen* server was used for the ligand parameterization of the lead compounds with OPLS-AA/1.14*CM1A as force field parameter (49). A 2-nanoseconds MDS was carried out for all the Apo and Holo structures with 1,000,000 steps after solvation, energy minimization and equilibration (NVT and NPT). MDS analyses of trajectory parameters such as the Root Mean Square Deviation of atomic positions (RMSD), per residue Root Mean Square Fluctuation (RMSF) of protein backbone, Principal Component Analysis (PCA) and Dynamical Cross-Correlation Matrix (DCCM), were determined using the BIO3D tool on the Galaxy super-computing platform (50).

RESULTS AND DISCUSSION

Structural analysis, validation and preparation of SARS-CoV-2 Helicase (QHD43415_12.pdb)

The Apo structure of SARS-CoV-2 Helicase (QHD43415_12.pdb) has 601 amino acids with the following constituent secondary structures: α helix 27%; beta sheets 31%; Coil 41%; and Turns 15%. (Figure 1).

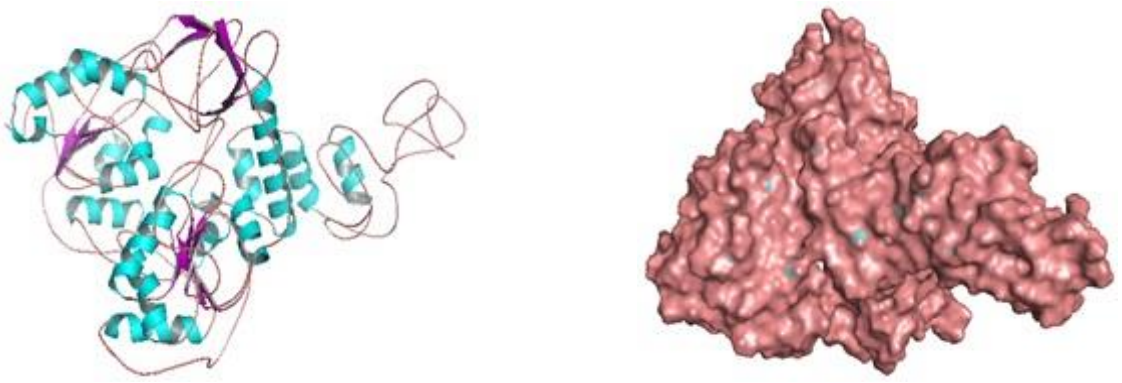

A B

Figure 1. (A) Cartoon model of the crystal structure of SARS-CoV-2 Helicase (QHD43415_12.pdb). Beta sheets (magentas), Alpha helix (cyan) and Loops (pink). (B) Surface representations.

The Total Accessible Solvent Area (ASA) is 26083.1 (Å) ². The geometry of SARS-CoV-2 Helicase (QHD43415_12.pdb) reveals 6.88% poor rotamers, 82.79% favored rotamers, 4.67% Ramachandran outliers, 85.48% Ramachandran favored, 3.34% Carbon Beta deviations >0.25Å, 0.00% bad bonds and 0.81% bad angles (Figure 2).

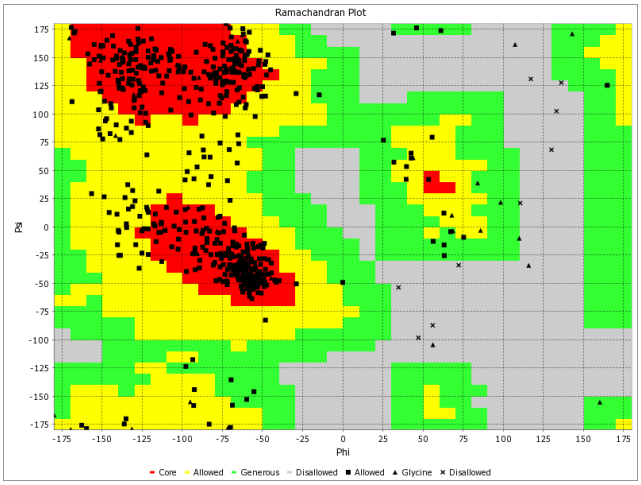

Figure 2. Ramachandran plot for SARS-CoV-2 Helicase (QHD43415_12.pdb).

The Peptide omegas of SARS-CoV-2 Helicase (QHD43415_12.pdb) include 0.00% Cis Prolines and 2.83% Twisted Peptides. The low-resolution criteria include 6.70% CaBLAM outliers and 0.34% CA Geometry outliers.

Chemoinformatic profile of ligands

The application of high-throughput computer-assisted approaches to predict the relationship between the chemical properties, structure and the biological activity of a compound is indeed a valuable tool in the field of drug design and discovery (51, 52, 53).

These drug-like properties of compounds would impart largely on their bioavailability and increase cellular uptake of biomolecules within the body. The molecular descriptors of such compounds are well described by the Lipinski (RO5), Veber, and Ghose rules. Put together, these rules state that hydrogen bond acceptors should be ≤ 10, hydrogen bond donors should be ≤ 5; Log P should be ≤ 5, molecular weight should be ≤ 500g/mol; the polar surface area should

be ≤ 140A²; molar refractivity should be between 40-130 cm³ and the number of rotatable bonds should be < 10 (54, 55, 56).

Our results prove that GA12, GA20 and GA51 had no violation of the Lipinski (RO5), Ghose and Veber rules suggesting that they possess good drug permeability (Figure 3, Table 1).

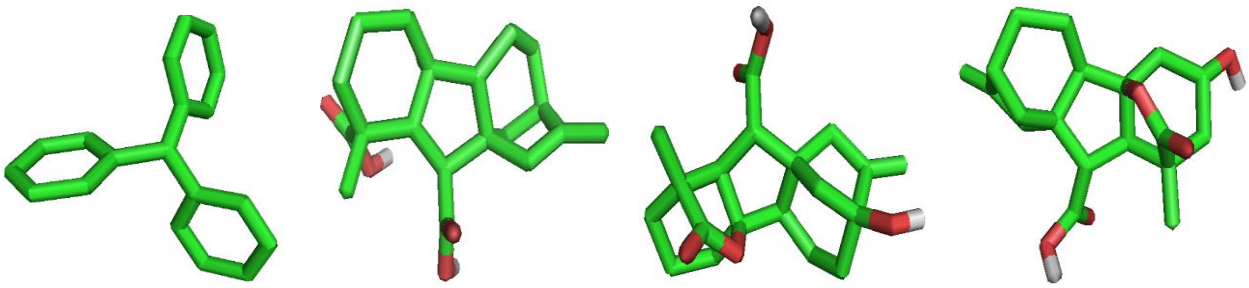

A B C D

Figure 3. The 3D chemical structures (stick model) of standard and lead compound. (A) Triphenylmethane, (B) GA12, (C) GA20 and (D) GA51.

Table 1. Chemoinformatic properties of standard and lead compounds

	Triphenylmethane	GA12	GA20	GA51
Molecular Formula	$C_{19}H_{16}$	$C_{20}H_{28}O_4$	$C_{19}H_{24}O_5$	$C_{19}H_{24}O_5$
Molecular Weight (g/mol)	244.3	332.4	332.4	332.4
Log P	5.3	3.9	1.2	1.7
Hydrogen Bond Acceptors	0	4	5	5
Hydrogen Bond Donors	0	2	2	2
# heavy atoms	19	24	24	24
# rotatable bonds	3	2	1	1
TPSA (A^a)	0	74.6	83.8	83.8

Molar Refractivity	80.38	0.8	0.79	0.79
Saturation (fraction csp^3)	0.05	90.52	86.18	86.14
PAIN Alert	0	0	0	0
GCPR ligand	-0.21	0.32	0.22	0.17
Ion channel modulator	-0.17	0.14	0.23	0.21
Kinase Inhibitor	-0.57	-0.44	-0.21	-0.31
Nuclear receptor ligand	-0.15	0.8	0.49	0.67
Protease inhibitor	-0.40	0.12	0.09	0.16
Enzyme inhibitor	-0.03	0.36	0.30	0.38

Specifically, the standard has a Log P value that violates the Lipinski rule. It is more lipophilic than all the lead compounds suggesting that it has the greatest absorbability across lipid membranes. The standard and the lead compounds can penetrate the Blood Brain Barrier because their TPSA values are less than 90 angstroms squared (57).

Measured by saturation, the molecular complexity of organic molecules is an important property in computational drug discovery. The lead compounds have their fraction of carbons in the sp3 hybridization more than 0.25 while that of the standard is lower. This suggests the standard has the lowest saturation and hence the least molecular stability (58).

In biological assays, certain compounds (PAINS: pan assay interference) yield false positive response because they have problematic structural moieties. These compounds are considered promiscuous as they are frequent hitters. From Table 1, the standard and all the lead compounds have no PAIN alerts (59). The bioactivity scores of the standard and the lead compounds showed moderate to good activity against ion channel, GCPR, nuclear receptor, kinase, proteases and other enzyme targets. The greatest enzyme inhibiting activity is seen in GA51 (60).

Pharmacokinetic properties of ligands

Traditional drug discovery process has bottlenecks. However, the application of *in silico* ADMET properties prediction to evaluate potential leads at early stages of drug development is important in order to eliminate candidates which would have been chemically synthesized and biologically tested (61). Multi-parametric optimization strategies such as absorption, distribution, metabolism, excretion/elimination and toxicity are applied in making and screening compounds in drug discovery (62).

The absorption parameters that ensure drugs get to their molecular targets include human intestinal absorption (poor: <30%), caco2 permeability (high: > 0.9), water solubility (insoluble: -4.0 Log mol/L), and skin permeability (low: LogKp >−2.5). Triphenylmethane is insoluble in water and therefore is a poor drug candidate (Table 2). All predicted absorption values for the lead compounds are within pharmacological range (57).

Table 2. Pharmacokinetic properties of front-runner compounds

	Triphenylmethane	GA12	GA20	GA51
Water solubility (log mol/L)	-6.884	-2.89	-2.636	-2.728
Caco2 permeability (log Papp in 10-6 cm/s)	1.536	1.052	1.186	1.136
Human Intestinal absorption (% Absorbed)	98.553	100	98.911	100
Skin Permeability (log Kp)	-2.707	-2.735	-2.735	-2.735
P-glycoprotein substrate (Yes/No)	Yes	No	No	No
P-glycoprotein I inhibitor (Yes/No)	No	No	No	No
P-glycoprotein II inhibitor (Yes/No)	No	No	No`	No
VDss (human) (log L/kg)	0.259	-1.324	-0.829	-0.969
Fraction unbound (human) (Fu)	0.157	0.22	0.418	0.286

BBB permeability (log BB)	0.854	0.074	-0.209	-0.091
CNS permeability (log PS)	-1.113	-2.08	-0.2998	-2.411
CYP2D6 substrate (Yes/No)	No	No	No	No
CYP3A4 substrate (Yes/No)	Yes	Yes	Yes	Yes
CYP1A2 inhibitor (Yes/No)	Yes	No	No	No
CYP2C19 inhibitor (Yes/No)	Yes	No	No	No
CYP2C9 inhibitor (Yes/No)	No	No	No	No
CYP2D6 inhibitor (Yes/No)	No	No	No	No
CYP3A4 inhibitor (Yes/No)	No	No	No	No
Total Clearance (log ml/min/kg)	0.201	0.4626	0.417	0.416
Renal OCT2 substrate (Yes/No)	No	No	No	No
AMES toxicity (Yes/No)	No	No	No	No
Max. Tolerated dose (human) (log mg/kg/day)	0.673	0.42	0.371	-0.135
hERG I inhibitor (Yes/No)	No	No	No	No
hERG II inhibitor (Yes/No)	Yes	No	No	No
Oral Rat Acute Toxicity (LD50) (mol/kg)	2.032	2.464	2.051	2.101
Oral Rat Chronic Toxicity (log mg/kg_bw/day)	0.822	2.074	2.135	2.364
Hepatotoxicity (Yes/No)	Yes	Yes	No	Yes
Skin Sensitization (Yes/No)	Yes	No	No	No
T. Pyriformis toxicity (log ug/L)	0.428	0.285	0.285	0.285
Minnow toxicity (log mM)	0.063	0.306	1.958	1.159

The pharmacokinetic indicators for distribution such as Fraction unbound, Volume of distribution steady state (Low: Log VDss <- 0.15; High: Log VDss > 0.45), BBB permeability (permeable: Log BBB > 0.3; poor <: Log BBB <-1), and CNS permeability (permeable Log PS >

-2; poor Log PS < -3) for standard and all lead compounds are within acceptable range (Table 2) (42, 63).

The standard and all lead compounds are not P-glycoprotein I & II inhibitors suggesting that these ATP-dependent cell membrane proteins would continue to pump foreign substances out of cells unhindered (Table 2). Triphenylmethane is a P-glycoprotein substrate which suggests it would be pumped out of the cell if it is not administered with a P-glycoprotein inhibitor (42, 64).

The inhibition of the major isoforms of cytochrome P450 enzyme makes for the toxic accumulation of their substrates. The predicted metabolic behavior of all the lead compounds shows no inhibition of CYP3A4, CYP1A2, CYP2C9, CYP2C19, and CYP2D6 enzymes. However, the standard shows inhibition of CYP1A2 and CYP2C19 enzymes (Table 2). The standard and lead compounds are substrates of CYP3A4 which means that their doses would be affected either by induction or the inhibition of CYP3A4 (65).

From Table 2, the predicted excretion values for Total Clearance for the standard and lead compounds are within pharmacological range (66). All of the lead compounds and the standard are not substrates of Renal Organic Cation Transporter 2 (OCT2) which implies that they will not be eliminated by the protein from the blood into the proximal tubular cell (67).

The dose to be administered in the phase 1 of clinical trials is determined by the predicted maximum recommended tolerated dose. From Table 2, the standard has a high value (more than 0.477 log mg/kg/day) while the lead compounds have low maximum recommended tolerated dose (less than 0.477 log mg/kg/day) (42).

Two important parameters in drug discovery are the *Tetrahymena pyriformis* and Minnow toxicities which are the dose required to inhibit 50% of the growth of *T.pyriformis* (IGC50), protozoan bacteria and the minnow fish respectively. For *T.pyriformis,* when the pIGC50 value is

greater than -0.5 log Ug/L, a compound is considered toxic. Therefore, the standard and all the leads show antibacterial properties but might not be toxic to human cells (42). Similarly, log LC50 is the log of a compound to cause death of 50% of flathead Minnows. A value less than 0.3 log mM signifies high acute toxicity. From the results, the standard is toxic to Minnows while the lead compounds are not (42).

The cardiotoxic and genotoxic properties of compounds is revealed by the HerG inhibition and AMES predictions respectively. While all the compounds (standard and leads) showed no AMES toxicity, only the standard showed hERG II inhibition properties. This make it a potentially dangerous drug candidate. The standard also showed dermatotoxic properties (42).

Molecular docking analyses of ligands against SARS-CoV-2 Helicase

In modern drug design and discovery, binding affinity determination is very crucial in order to find a high affinity ligand that would bind to the target protein to inhibit its disease-associated function, catalytic activity or interaction with other molecules (68). This procedure typically begins with screening an initial library of compounds to computationally identify binders of the target protein before continuing with the experimental screening (69). Successful hits are characterized and further developed.

From Figure 4 and Table 3, all lead compounds have stronger binding affinity than the standard and hence showed greater potency as drug candidates. GA A51 has the strongest binding affinity of -8.6 Kcal/mol.

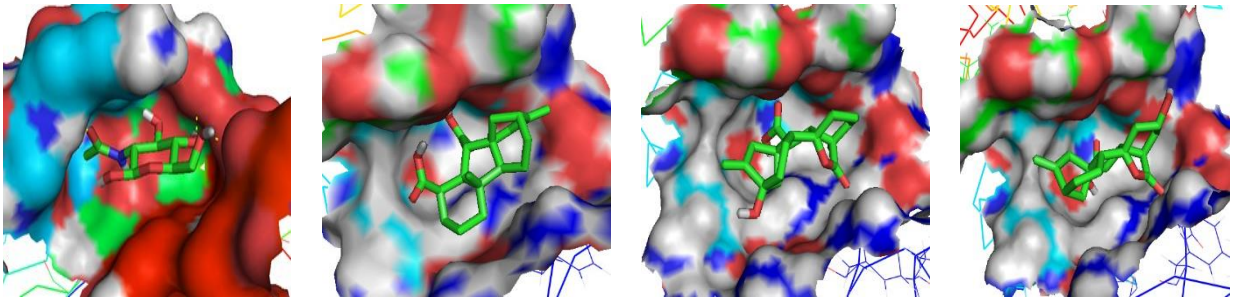

A B C D

Figure 4. Binding site of SARS-CoV-2 Helicase interacting with standard and lead compounds. (A) Helicase-Triphenylmethane complex, (B) Helicase-GA12 complex, (C) Helicase-GA20 complex and (D) Helicase-GA51 complex.

Table 3. Molecular docking scores of ligands against SARS-CoV-2 Helicase

Ligand	Binding (Kcal/mol) affinity
Triphenylmethane	-7.4
Gibberellin A12	-8.0
Gibberellin A20	-8.4
Gibberellin A51	-8.6

Binding Site analyses

Hydrogen bonds have ubiquitous influence in nature and play an important role in protein folding, protein-ligand interactions and catalysis (70, 71, 72). By displacing protein-bound water molecules into the solvent, H-bonds also enhances ligand binding affinity (73). The length and orientation of the hydrogen bond are two key factors that determine the specificity and direction of ligand binding (74).

Figure 5 and Table 4 reveal that while the standard has no hydrogen bond, GA12, GA20 and GA51 all have hydrogen bonds with residues that fall within Pocket 26. GA12 forms 3 hydrogen bonds within one residue (LEU235) while GA20 and GA51 form two hydrogen bonds within two residues (PHE24 & PHE133) signifying greater stability.

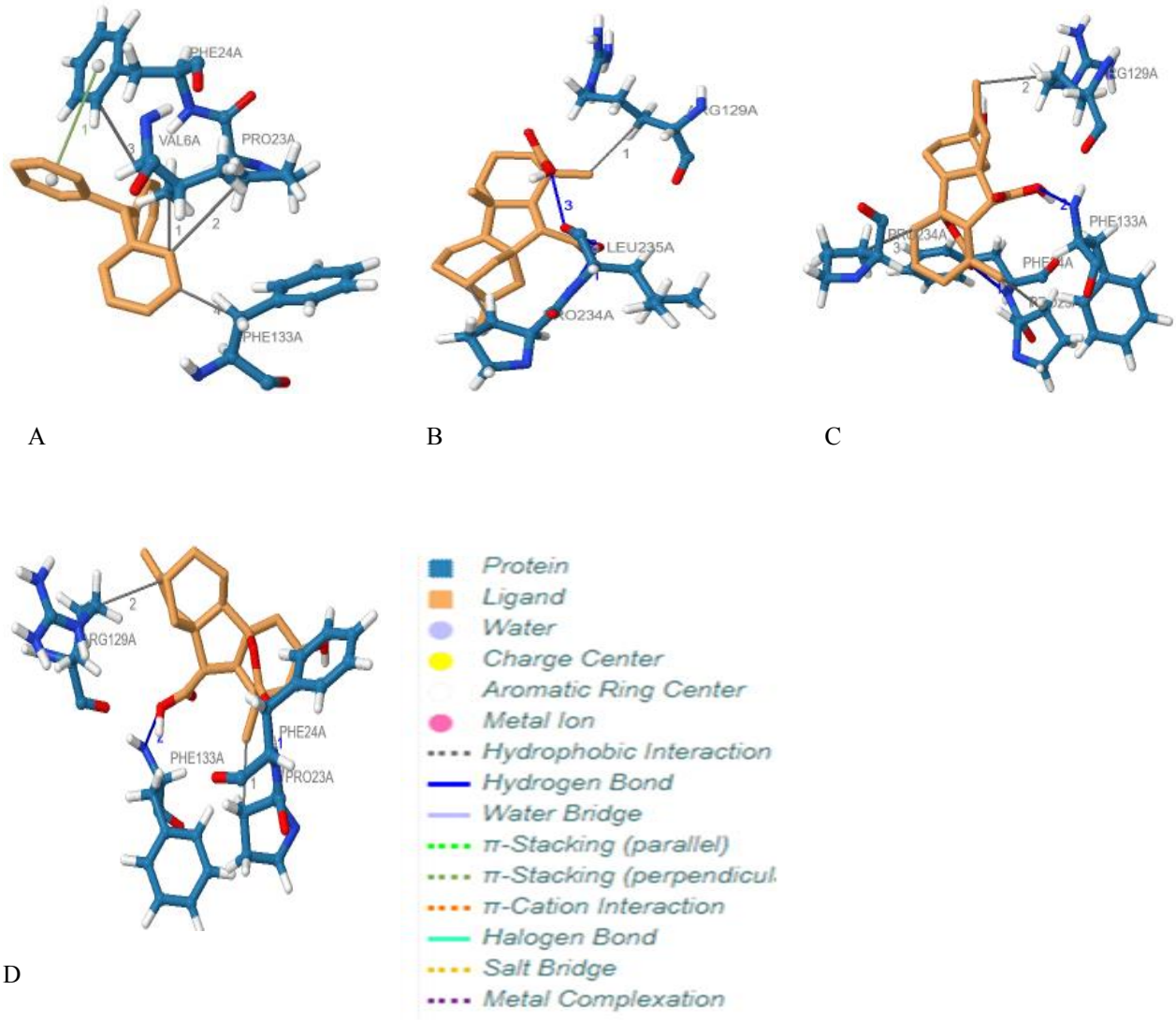

A B C

D

Figure 5. Protein-Ligand interactions of SARS-CoV-2 Helicase with standard and lead compound. (A) Helicase-Triphenylmethane complex, (B) Helicase-GA12 complex, (C) Helicase-GA20 complex and (D) Helicase-GA51 complex.

Table 4. Hydrogen bond analysis

Complex	Number of bonds	Residues	Distance (H-A)	Distance (D-A)	Bond angle
Hel-Triphenylmethane	0				
Hel-GA12	3	LEU235	3.22	4.01	134.88
		LEU235	2.24	3.09	145.5
		LEU235	2.76	3.16	105.78
Hel-GA20	2	PHE24	2.22	3.18	159.23
		PHE133	2.64	3.03	102.66
Hel-GA51	2	PHE24	2.09	3.06	159.85
		PHE133	2.83	3.31	109.57

In terms of angle formed by hydrogen bonds, GA12 forms two strong (greater than 130°) and one weak (less than 130°) hydrogen bonds with the target protein. GA20 and GA51 form one weak and one strong hydrogen bond each. (75). In terms of the donor to acceptor distance, GA12 forms two moderate (2.5-3.2 Å) and one weak (3.2-4.0 Å) hydrogen bonds with the target protein. GA20 forms two moderate hydrogen bonds while GA51 forms one moderate and one weak hydrogen bond (75).

The strength and stability of the protein-ligand complexes is enhanced by the presence of hydrophobic interactions and salt bridges (76). From Table 5, the standard forms 4 hydrophobic interactions and one strong salt bond (77).

Table 5. Other Protein-ligand interactions

	Hydrophobic Int.		Salt bridge		p-Stacking	
Complex	Residue	Distance	Residue	Distance	Residue	Distance
Hel-Triphenylmethane	VAL6	3.45			PHE24	4.86
	PRO23	3.90				
	PHE24	3.98				
	PHE133	3.63				
Hel-GA12	ARG129	3.60				
	PRO234	3.60				
Hel-GA20	PRO23	3.50				
	ARG129	3.86				
	PRO234	3.94				
Hel-GA51	PRO23	3.67				
	ARG129	3.99				

GA12 and GA51 forms 2 hydrophobic interactions and no salt bridge. GA20 forms 2 hydrophobic interactions and no salt bridge. These suggest that for the other protein-ligand interactions, the standard have a slightly more atom-efficient binding than the lead compounds (78, 79).

Put together, the lead compounds show a stronger interaction with SARS-CoV-2 Helicase as revealed by the hydrogen bonds and binding affinity scores.

Molecular Dynamics Simulation Analyses

Structures

As seen in Figures 1 and 6, comparing the crystal structure with the simulated apo and holo structures suggests that there is an unfolding of the alpha helix at residues 64, 65 and 66 during the molecular dynamic simulation (80).

A B C D E

Figure 6. Cartoon model of the crystal structure of SARS-CoV-2 Helicase Apo and Holo structures (without water and ions) after molecular dynamics simulation. Beta sheets (magenta), Alpha helix (cyan) and Loops (pink). (A) Helicase, (B) Helicase-Triphenylmethane complex, (C) Helicase-GA12 complex, (D) Helicase-GA20 complex and (E) Helicase-GA51 complex

Root Mean Square Deviation of Atomic Positions (RMSD)

RMSD is the measure of similarity between a reference and a target structure. It measures the variations in the distances between atoms in two superimposed protein structures. In protein structure prediction, RMSD is used for analysing protein stability and conformational changes. It describes the similarity of conformers (81, 82).

Figure 7 and Table 6 suggest that there was a gradual increase in the RMSD of the simulated Apo protein relative to the crystal as the production time increased. It peaked at Frame 9 (2.42 Å) and thereafter stabilized.

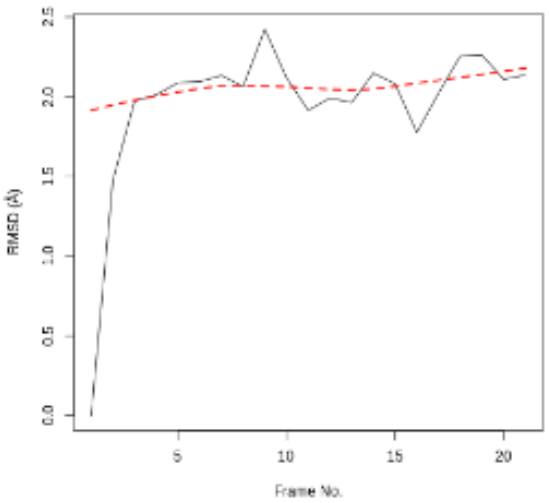
RMSD (Å)
0.0
0.5
1.0
1.5
2.0
2.5
5
10
15
20
Frame No.

A

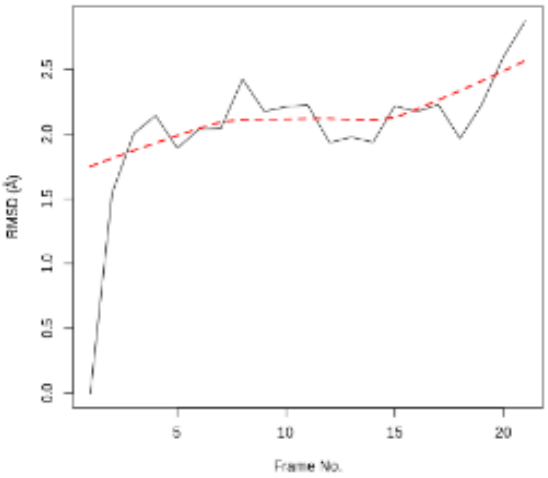
RMSD (Å)
0.0
0.5
1.0
1.5
2.0
2.5
5
10
15
20
Frame No.

B

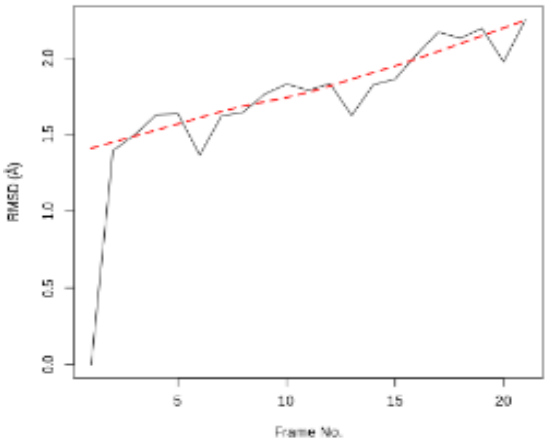
RMSD (Å)
0.0
0.5
1.0
1.5
2.0
5
10
15
20
Frame No.

C

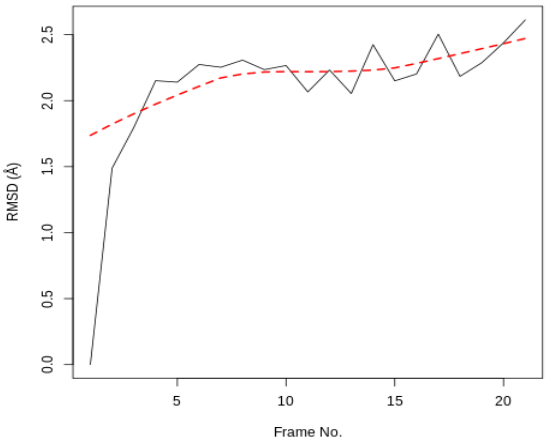
RMSD (Å)
0.0
0.5
1.0
1.5
2.0
2.5
5
10
15
20
Frame No.

D

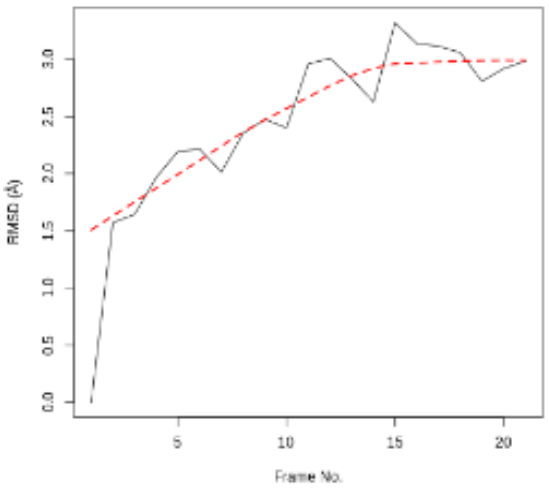

E

Figure 7. RMSD for Apo and Holo structures. (A) Helicase, (B) Helicase-Triphenylmethane complex, (C) Helicase-GA12 complex, (D) Helicase-GA20 complex and (E) Helicase-GA51 complex.

Table 6. Summary of data from Molecular Dynamics Simulations of Apo and Holo Structures

MDS Parameters	Helicase	Helicase-Triphenylmethane	Helicase-GA12	Helicase-GA20	Helicase-GA51
RMSD					
Total RMSD	41.05	42.84	36.06	44.06	51.06
Average RMSD	1.95	2.04	1.72	2.10	2.46
Lowest RMSD	0.00	0.00	0.00	0.00	0.00
Highest RMSD	2.42	2.87	2.25	2.61	3.32
Time Frame of Highest RMSD	1	1	1	1	1
Time Frame of Lowest RMSD	9	21	21	21	15

RMSD Peak Distribution					
0.00 - 0.49A	1	1	1	1	1
0.50 – 0.99A	0	0	0	0	0
1.00 – 1.49A	1	0	2	1	0
1.50 – 1.99A	5	6	13	1	3
2.00 – 2.49A	14	12	5	16	6
2.50 – 2.99A	0	2	0	2	6
3.00 – 3.49A	0	0	0	0	5
RMSF					
Total Global RMSF	598.93	639.76	610.30	622.78	724.06
Average Global RMSF	1.00	1.06	1.02	1.04	1.20
Total Regional (Pocket 26) RMSF	8.33	8.20	7.21	8.25	8.57
Average Regional (Pocket 26) RMSF	0.76	0.75	0.66	0.75	0.78
Least Fluctuation	0.45	0.44	0.45	0.40	0.39
Highest Fluctuation	3.48	3.52	2.83	4.06	4.37
Range of RMSF	3.03	3.08	2.38	3.66	3.98
PCA					
Total global motions (mean of PC1, PC2 & PC3)	20.57	19.20	20.3	20.7	20.9
Average global motions (mean of PC1, PC2 & PC3)	0.03	0.03	0.03	0.03	0.03
Total Regional (Pocket 26) Motion (mean of PC1, PC2 & PC3)	0.27	0.23	0.24	0.24	0.25

Average Regional (Pocket 26) Motion (mean of PC1, PC2 & PC3)	0.02	0.02	0.02	0.02	0.02
Best global Conformation	PC3	PC1	PC2	PC3	PC3
Best regional Conformation (Pocket 26)	PC3	PC3	PC1	PC1	PC3
PC1 Eigenvalue	19.90%	30.70%	31.70%	30.70%	50.20%
PC2 Eigenvalue	15.70%	0.16	14.50%	20.50%	10.50%
PC3 Eigenvalue	13.30%	0.13	9.20%	9.30%	8.50%
Total	48.90%	59.80%	55.40%	60.50%	69.20%
PC1 cosine content	0.87	0.86	0.82	0.87	0.87
PC2 cosine content	0.23	0.32	0.71	0.76	0.87
PC3 cosine content	0.13	0.34	0.70	0.53	0.68

Throughout the trajectory, the total RMSD for the Apo structure is 41.05 Å while the average is 1.95 Å. While the RMSD values of the Apo protein appear to have stabilized with the simulation time, data suggests that with more simulation time, the RMSD values for all the holo structures would increase. Of all the holo structures, the Helicase-GA51 complex has the greatest deviation from the reference structure. This is seen in the highest values of the total and average RMSD. Helicase-GA12 and Helicase-Triphenylmethane complexes have lower total and average RMSD values than the Helicase-GA20. The Helicase-GA51 complex showed the greatest deviation to the right (most peaks within 2.00 - 2.49A). The Helicase-GA20 complex also showed greater deviation to the right than the Helicase-GA12 complex which in turn was greater than the Helicase-Triphenylmethane complex (Figure 8 and Table 6).

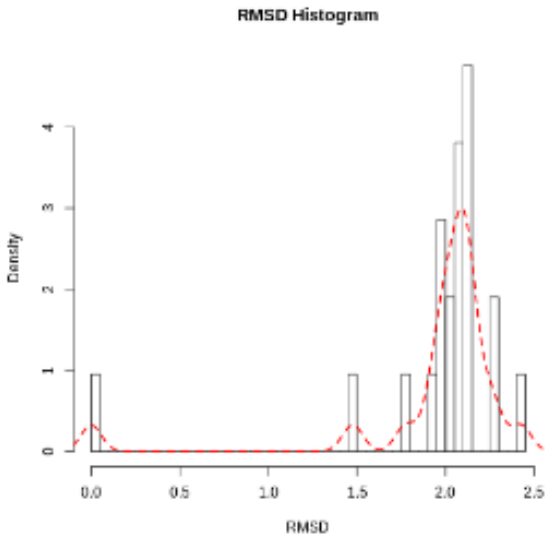
RMSD Histogram
Density
RMSD
0.0
0.5
1.0
1.5
2.0
2.5
0
1
2
3
4

A

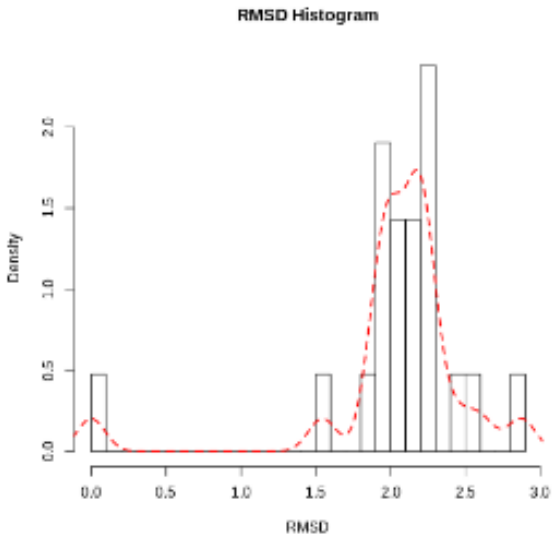
RMSD Histogram
Density
RMSD
0.0
0.5
1.0
1.5
2.0
2.5
3.0
0.0
0.5
1.0
1.5
2.0

B

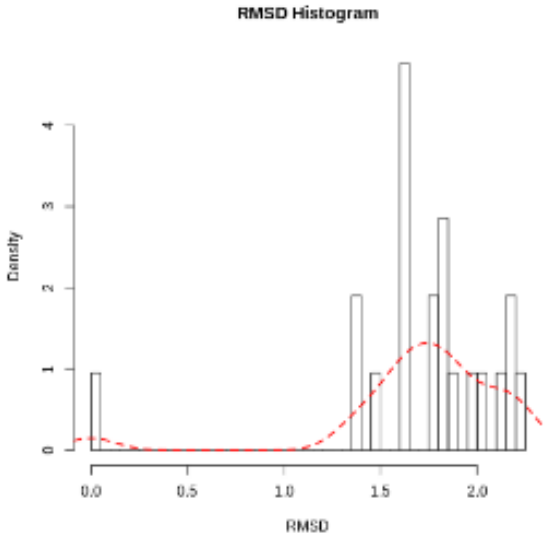
RMSD Histogram
Density
RMSD
0.0
0.5
1.0
1.5
2.0
0
1
2
3
4

C

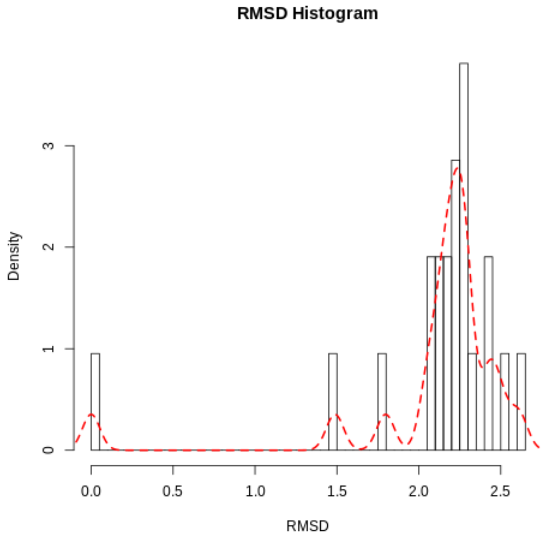
RMSD Histogram
Density
RMSD
0.0
0.5
1.0
1.5
2.0
2.5
0
1
2
3

D

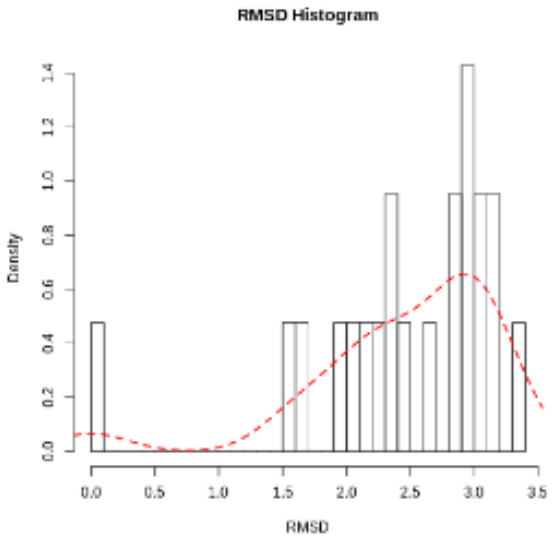

E

Figure 8. RMSD histogram for Apo and Holo structures. (A) Helicase, (B) Helicase-Triphenylmethane complex, (C) Helicase-GA12 complex, (D) Helicase-GA20 complex and (E) Helicase-GA51 complex.

Put together, ligand binding with GA51 and GA20 appear to cause greater deviation from the reference structure than Triphenylmethane. The least deviation was induced by GA12. The results predict GA51 to cause the greatest structural deviation of all the holo structures.

Root Mean Square Fluctuations (RMSF)

Proteins undergo structural fluctuations as a result of movements of the alpha carbon of their residues around their equilibrium conformations (83). From Figure 9 and Table 6, the total and average global RMSF is greater in the Helicase-GA51 complex than all the other holo structures. While the total and average global RMSF values of the Helicase-Triphenylmethane complex is greater than those of the Helicase-GA12 and Helicase-GA20 complexes.

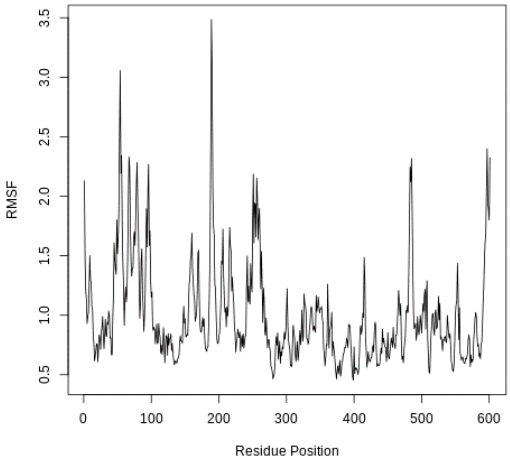
RMSF
0.5
1.0
1.5
2.0
2.5
3.0
3.5
0
100
200
300
400
500
600
Residue Position

A

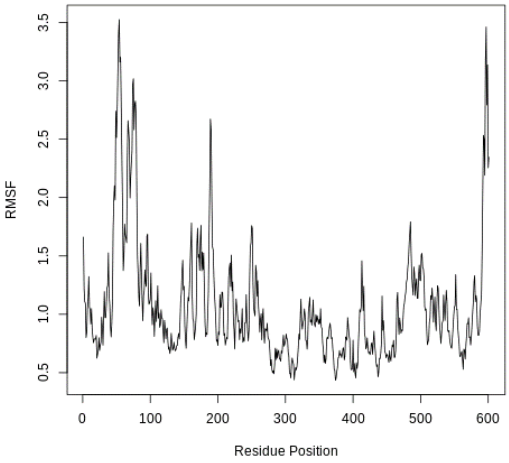
RMSF
0.5
1.0
1.5
2.0
2.5
3.0
3.5
0
100
200
300
400
500
600
Residue Position

B

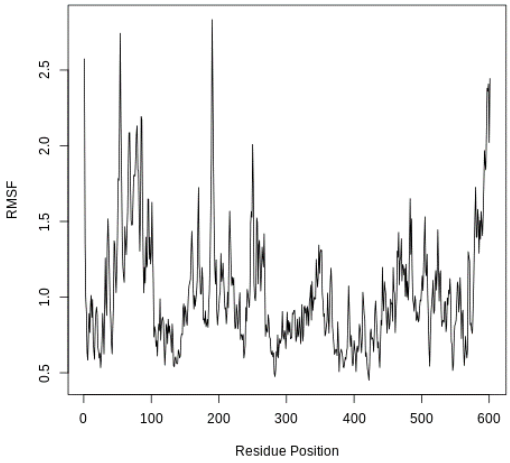
RMSF
0.5
1.0
1.5
2.0
2.5
0
100
200
300
400
500
600
Residue Position

C

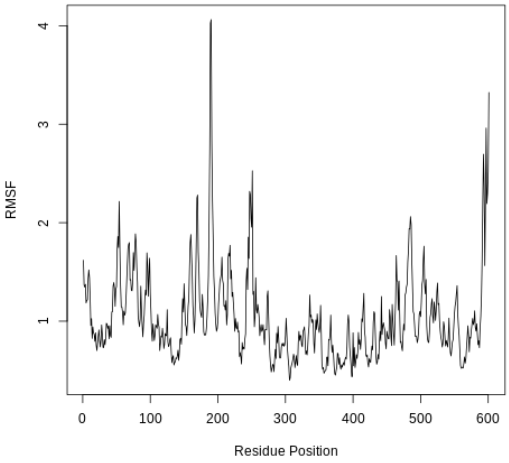
RMSF
1
2
3
4
0
100
200
300
400
500
600
Residue Position

D

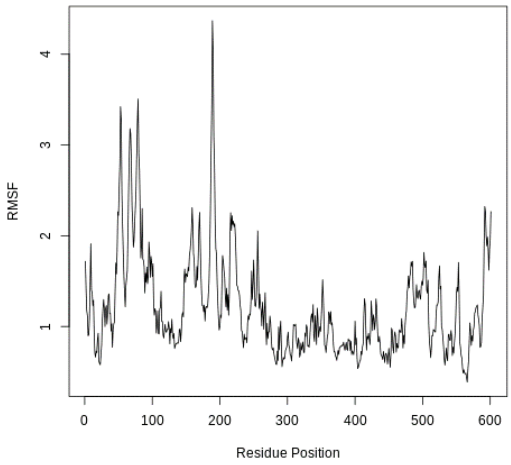

E

Figure 9. Per-residue RMSF for Apo and Holo structures. (A) Helicase, (B) Helicase-Triphenylmethane complex, (C) Helicase-GA12 complex, (D) Helicase-GA20 complex and (E) Helicase-GA51 complex.

The total and average regional RMSF values at Pocket 26 remained highest for the Helicase-GA51 complex. The values for Helicase-GA20 complex was higher than those of the Helicase-Triphenylmethane complex. The Helicase-GA12 complex has the lowest values. Similarly, the range of RMSF followed the same order with Helicase-GA51 and Helicase-GA20 complexes having the highest values.

Put together, ligand binding with GA51 induced the greatest instability as seen in the global, regional RMSF values and the range of RMSF. Ligand binding with GA20 also induced more instability of the SARS-CoV-2 Helicase than the standard.

Principal components Analysis

During the MDS of a protein, new conformations are been generated during the trajectory. Principal component analysis (PCA) is used to determine the statistical significance and relationships of these conformations (84).

Of all the holo structures, the Total global motions (average of PC1, PC2 and PC3) was highest in Helicase-GA51 complex. Also, Helicase-GA20 and Helicase-GA12 complexes showed greater global motion than the Helicase-Triphenylmethane complex (Figure 10 and Table 6).

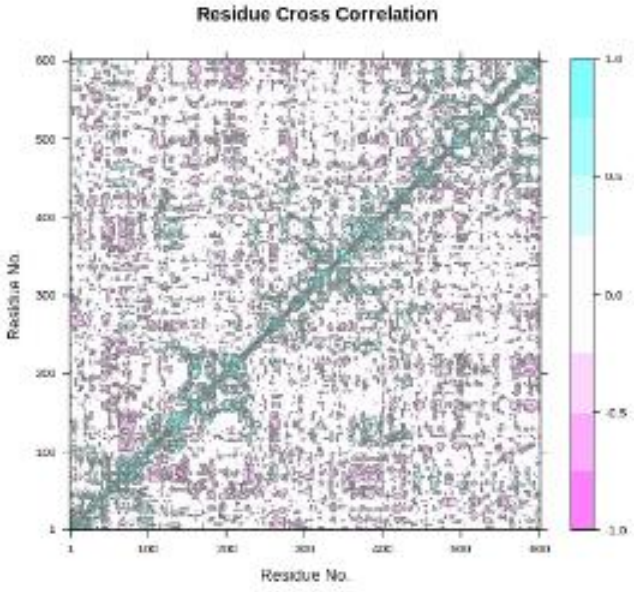
Residue Cross Correlation
Residue No.
Residue No.

A

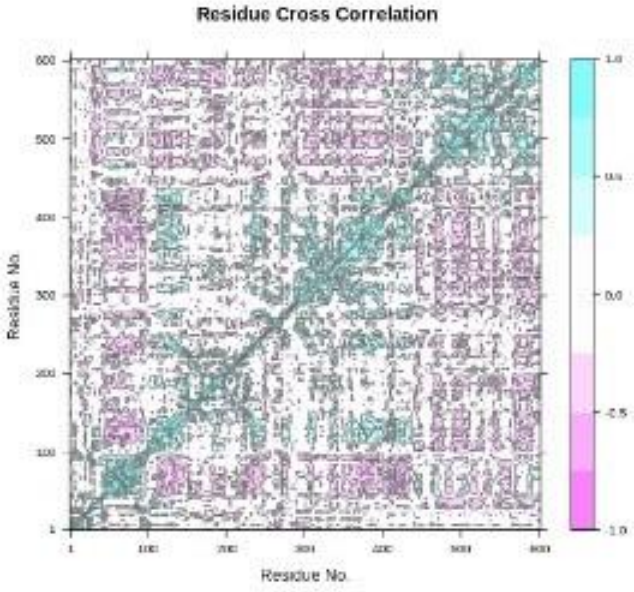
Residue Cross Correlation
Residue No.
Residue No.

B

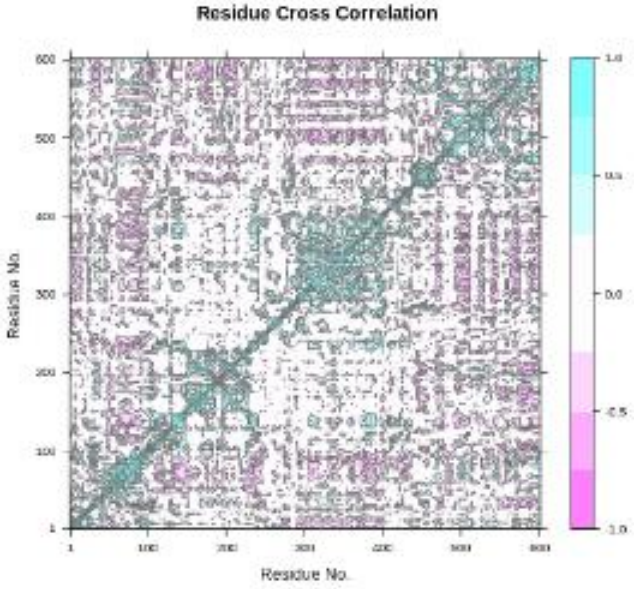
Residue Cross Correlation
Residue No.
Residue No.

C

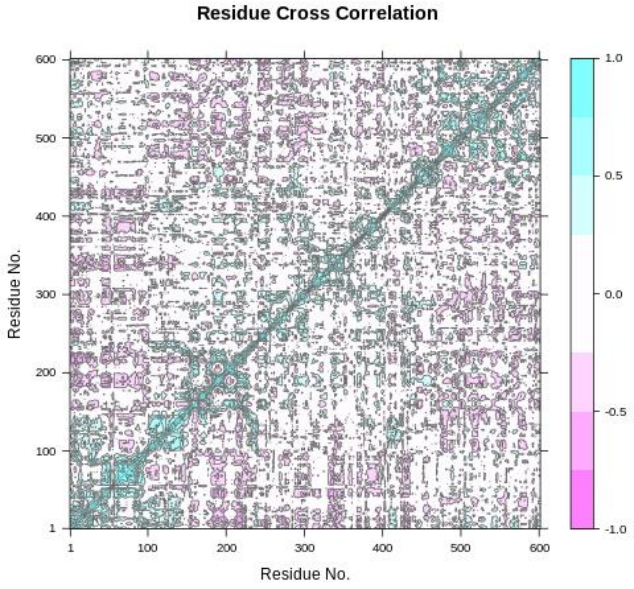
Residue Cross Correlation
Residue No.
Residue No.

D

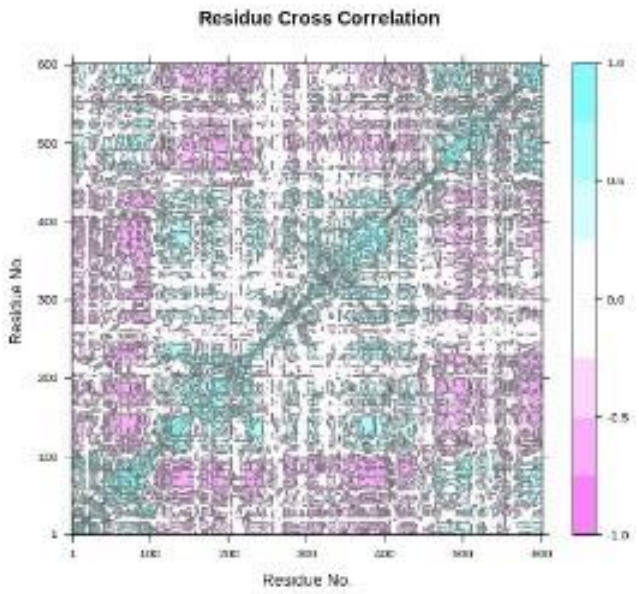

E

Figure 10. Dynamic cross correlation map Apo and Holo structures of SARS-CoV-2 Helicase. Purple represents anti-correlated, dark cyan represents fully correlated while white and cyan represents moderately and uncorrelated respectively. 1.0= correlated; 0 is non-correlated; and 1 is anti-correlated. (A) Helicase, (B) Helicase-Triphenylmethane complex, (C) Helicase-GA12 complex, (D) Helicase-GA20 complex and (E) Helicase-GA51 complex.

In a similar manner, the Total regional motions (average of PC1, PC2 & PC3) was highest in Helicase-GA51 complex making it the most unstable at Pocket 26 of all the holo structures.

Based on the greatest motions, the best global conformations are PC3 of the Apo protein, PC1 of Helicase-Triphenylmethane complex, PC2 of Helicase-GA12 complex, PC3 of the Helicase-GA20 complex and PC3 of the Helicase-GA51 complex. Similarly, the best conformations that produced the greatest motions at Pocket 26, are PC3, PC3, PC1, PC1 and PC3 of the Apo

protein, Helicase-Triphenylmethane, Helicase-GA12, Helicase-GA20 and Helicase-GA51 complexes respectively.

The cosine contents of the principal components reveal the convergence of the MD simulation. Monitoring convergence is essential for sampling quality as results should be accurate and reproducible. Table 6 shows good quality cosine content data except a slight non-convergence at the PC3 of the Helicase- Triphenylmethane complex (85).

Put together, while all lead compounds induced greater motions of the SARS-CoV-2 Helicase than the standard, GA51 induced the greatest motions. This implies that GA51 would induce the greatest structural distortion of the viral protein at global and regional (Pocket 26) levels.

Dynamic Cross Correlation Map (DCCM)

DCCM is a widely accepted tool used to analyze trajectories of molecular dynamics simulation. It is used to calculate the time-correlation atom motion of a system as it reveals the heat map of the cross correlation of residual fluctuations (86, 87).

Figure 11 and Table 6, shows heat maps depicting a complex pattern of correlated, non-correlated and anti-correlated motions in Apo and Holo structures.

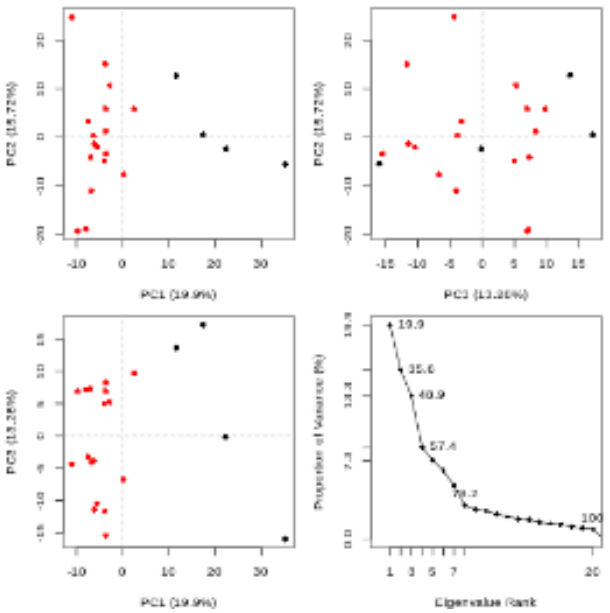
PC1 (19.9%)
PC2 (15.72%)
PC2 (13.28%)
PC3 (13.28%)
Proportion of Variance (%)
Eigenvalue Rank
19.9
35.6
48.9
57.4
68.2
100

A

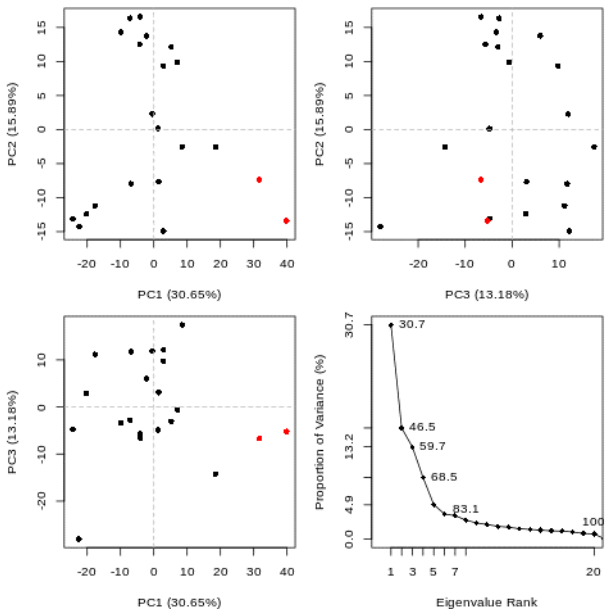
PC1 (30.65%)
PC2 (15.89%)
PC3 (13.18%)
Proportion of Variance (%)
Eigenvalue Rank
30.7
46.5
59.7
68.5
83.1
100

B

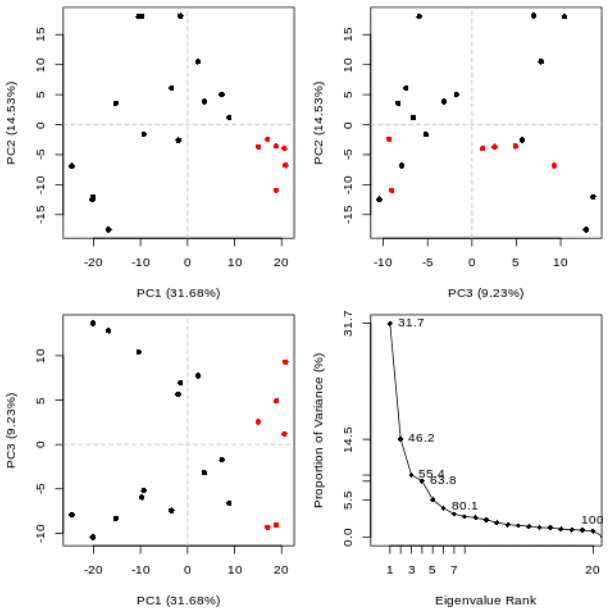
PC1 (31.68%)
PC2 (14.53%)
PC3 (9.23%)
Proportion of Variance (%)
Eigenvalue Rank
31.7
46.2
55.4
63.8
80.1
100

C

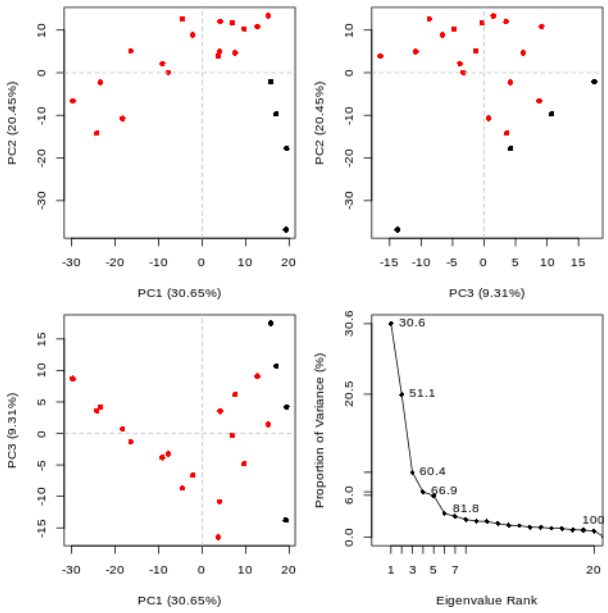
PC1 (30.65%)
PC2 (20.45%)
PC3 (9.31%)
Proportion of Variance (%)
Eigenvalue Rank
30.6
51.1
60.4
66.9
81.8
100

D

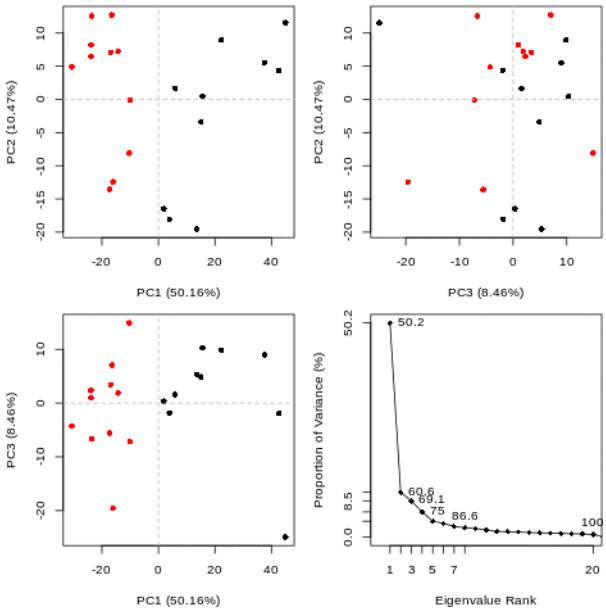

E

Figure 11. Principle component analysis cluster plot of Apo and Holo structures. The projection of trajectory onto 1st three eigenvectors for: (A) Helicase, (B) Helicase-Triphenylmethane complex, (C) Helicase-GA12 complex, (D) Helicase-GA20 complex and (E) Helicase-GA51 complex.

Comparative results reveal that atomic motions in the Helicase- GA51 complex showed the most intense anti-correlated motions in the holo structures. The Helicase-Triphenylmethane complex has predominantly non-correlated motions in residues 1-300. On the contrary, the Helicase-GA51 complex has predominantly correlated motions between residues 1-100 and non-correlated motions between residues 100-300. While the heat map of the Helicase-GA12 complex closely resembles that of the Helicase-Triphenylmethane, that of the Helicase-GA20 complex is less intense than that of the Helicase-GA51 complex with respect to anti-correlation motions.

Put together, the standard and all the lead compounds induced anti-correlation motions on SARS-CoV-2 Helicase. GA51 induced the greatest anti-correlation motions.

CONCLUSION

The standard and lead compound

Triphenylmethane and its derivatives are a group of dyes which include bromocresol green, malachite green, methyl violet, Victoria blue, and Fuchsine. Triphenylmethane derivatives have been shown to be toxic to different organisms which includes the Coronaviridae, Picornaviridae and Flaviviridae families of viruses (26, 27).

Found abundantly in *Pisum sativum* (green peas) and *Abelmoschus esculentus* (okra), Gibberellins (GAs) are plant hormones that regulate its various physiological processes (88,89). Notably in cucumbers, the Mosaic virus infection is associated with a reduced concentration of endogenous gibberellins which culminates in stunted roots and reduced leaf and stem growth (90).

During this study, the molecular docking simulations reveal that while GA29 binds at the active site, GA44, GA53, GA29 catabolite and GA27 bind at other pockets which are probable allosteric sites. This suggests that the *in vitro* antiviral activities of GAs should be investigated. GA29 and GA20 are also predicted to be good drug candidates and have a modulatory effect on killer cell immunoglobulin-like receptor 2DS2 of Natural Killer Cells (91). Similarly, GAs have been implicated as modulators of plant innate immunity (92).

Summary of comparative analyses

A thorough evaluation of the chemoinformatic and pharmacokinetic profiles of the standard and lead compounds reveal the choice of ideal drug candidates against SARS-CoV-2 Helicase.

With a slightly higher Log P value than the Lipinski rule range, the standard shows more lipophilicity than the lead compounds. Also, the standard is predicted to be insoluble in water (log mol/L= 6.884), a substrate of P-glycoprotein, toxic to flathead Minnow fish (log mM=0.063), inhibit cardiac ion channel protein, hERG II, causes skin sensitization and inhibits CYP1A2 and CYP2C19 enzymes. Though Triphenylmethane has been proven to be a viral Helicase inhibitor, it is a poor drug candidate and it is used as a synthetic dye (26, 27).

On the contrary, the lead compounds are all good drug candidates. They are all substrates of the CYP3A4 and this suggests that they should be administered with an inhibitor of that enzyme.

GA51 is predicted to have the highest enzyme inhibiting activity and also the strongest binding affinity (-8.6 Kcal/mol) for SARS-CoV-2 Helicase. The other lead compounds showed a greater binding affinity than the standard which had no hydrogen bond with the target protein. Studying the time-resolved motions of Apo and Holo macromolecules, GA51 and GA20 are predicted to have better pharmacodynamics than the standard. The standard proved to be better than GA12. Specifically, as a viral protein inhibitor, GA51 and GA20 show greater structural distortion to the SARS-CoV-2 Helicase as seen in the RMSD values, distribution of RMSD peaks, RMSF, and PCA (global and local motions) than the standard. Overall GA51 has been predicted to show the greatest SARS-CoV-2 Helicase inhibitory activity as further confirmed by the DCCM map.

It is recommended that further investigation be carried out to evaluate the inhibitory activity of GA51 and GA20 against SARS-CoV-2 Helicase using *in vivo* and *in vitro* experiments.

Conflict of Interest

None

Author Contributions

The manuscript was written through contributions of all authors. All authors have given approval to the final version of the manuscript.

ACKNOWLEDGMENT

We wish to express our gratitude to the administration of Medical Biotechnology Department, National Biotechnology Development Agency, Abuja, Nigeria for providing a suitable environment for this research.

ABBREVIATIONS

COVID-19, coronavirus disease 2019; SARS-CoV-2, severe acute respiratory syndrome coronavirus 2; MDS, molecular dynamics simulations; ADMET, absorption, distribution, metabolism, excretion and toxicity.

REFERENCES

1. World Health Organization. Coronavirus disease (COVID-19) situation report – 86. https://www.who.int/docs/default-source/coronaviruse/situation-reports/20200415-sitrep-86-covid-19.pdf?sfvrsn=c615ea20_6, 2020 (accessed 15 April 2020).

2. Huang, C.; Wang, Y.; Li, X.; Ren, L.; Zhao, J.; Hu, Y.; Zhang, L.; Fan, G.; Xu, J.; Gu, X.; Cheng, T. Yu, J. Xia, Y. Wei, W. Wu, X. Xie, W. Yin, H. Li, M. Liu, Y. Xiao, H. Gao, L. Guo, J. Xie, Z.; Wang, G.; Jiang, R.; Gao, Z.; Jin, Q.; Wang, J.; Cao, B. Clinical

features of patients infected with 2019 novel coronavirus in Wuhan, China. *Lancet.* **2020**, *395*, 497–506. https://doi.org/10.1016/S0140-6736(20)30183-5.

3. Lin, S. Y.; Liu, C. L.; Chang, Y.-M.; Zhao, J.; Perlman, S.; Hou, M. H. Structural basis for the identification of the N-terminal domain of coronavirus nucleocapsid protein as an antiviral target. *J. Med. Chem.* **2014**, *57*, 2247–2257. https://doi.org/10.1021/jm500089r.

4. Shimamoto, Y., Hattori, Y., Kobayashi, K., Teruya, K., Sanjoh, A., Nakagawa, A., Yamashita, E., Akaji, K. Fused-ring structure of decahydroisoquinolin as a novel scaffold for SARS 3CL protease inhibitors. *Bioorg. Med. Chem.* **2015**, *23*, 876–890. https://doi.org/10.1016/j.bmc.2014.12.028.

5. Hilgenfeld, R. From SARS to MERS: crystallographic studies on coronaviral proteases enable antiviral drug design. FEBS J. **2014**, *281*, 4085–4096. https://doi.org/10.1111/febs.12936.

6. Chang, C. Y.; Chang, C. P.; Chakraborty, S.; Wang, S. W.; Tseng, Y. K.; Wang, C. C. Modulating the Structure and Function of an Aminoacyl-tRNA Synthetase Cofactor by Biotinylation. *J. Biol. Chem.* **2016**, *291*, 17102–17111. https://doi.org/10.1074/jbc.M116.734343.

7. Paules, C. I., Marston, H. D., Fauci, A. S. Coronavirus Infections—More Than Just the Common Cold. *JAMA.* **2020**, *323*, 707–708. https://doi.org/10.1001/jama.2020.0757.

8. Alsaadi, J. E.; Jones, I. M. Membrane binding proteins of coronaviruses, *Future Virol.* **2019**, 14, 275–286. https://doi.org/10.2217/fvl-2018-0144.

9. Crute, J. J.; Grygon, C.A.; Hargrave, K.D.; Simoneau, B.; Faucher, A.M.; Bolger, G.; Kibler, P.; Liuzzi, M.; Cordingley, M. G. Herpes simplex virus helicase-primase inhibitors are active in animal models of human disease. *Nat. Med.* ***2002,*** *8*, 386–391. https://doi.org/10.1038/nm0402-386.

10. Marra, M.A.; Jones, S.J.M.; Astell, C.R.; Holt, R.A.; Brooks-Wilson, A.; Butterfield, Y.S.N.; Khattra, J.; Asano, J.K.; Barber, S.A.; Chan, S.Y.; and et al. The Genome sequence of the SARS-associated coronavirus. *Science*. **2003**, *300*, 1399–1404. https://doi.org/10.1126/science.1085953.

11. Nicholls, J. M.; Poon, L. L. M.; Lee, K. C.; Ng, W. F.; Lai, S. T.; Leung, C. Y.; Chu, C.M.; Hui, P.K.; Mak, K.L.; Lim, W.; and et al. Lung pathology of fatal severe acute respiratory syndrome. *Lancet,* **2003**, *361,* 1773–1778. https://doi.org/10.1016/s0140-6736(03)13413-7.

12. Bosch, B. J.; van der Zee, R.; de Haan, C. A. M.; Rottier, P. J. M. The coronavirus spike protein is a class I virus fusion protein: structural and functional characterization of the fusion core complex. *J. Virol*. **2003**, *77*, 8801–8811. https://doi.org/10.1128/jvi.77.16.8801-8811.2003.

13. Fung, T. S.; Liu, D. X. Human Coronavirus: Host-Pathogen Interaction. *Annu. Rev. Microbiol.* **2019**, *73*, 529–557. https://doi.org/10.1146/annurev-micro-020518-115759.

14. Yu, F.; Du, L.; Ojcius, D. M.; Pan, C.; Jiang, S. Measures for diagnosing and treating infections by a novel coronavirus responsible for a pneumonia outbreak originating in Wuhan, China. *Microbes Infect.* **2020**, *22*, 74–79. https://doi.org/10.1016/j.micinf.2020.01.003.

15. Yedavalli, V.S.; Neuveut, C.; Chi, Y.H; Kleiman, L.; Jeang, K.T. Requirement of DDX3 DEAD box RNA helicase for HIV-1 Rev-RRE export function. *Cell.* **2004**, 119, 381–392. https://doi.org/10.1016/j.cell.2004.09.029.

16. Richardson, J.P. Loading Rho to terminate transcription., *Cell.* **2003**, *114*, 157–159. https://doi.org/10.1016/s0092-8674(03)00554-3.

17. Kusakabe, T.; Hine, A.V.; Hyberts, S.G.; Richardson, C.C. The Cys4 zinc finger of bacteriophage T7 primase in sequence-specific single-stranded DNA recognition. *Proc. Natl. Acad. Sci. U.S.A.* **1999**, *96*, 4295–4300. https://doi.org/10.1073/pnas.96.8.4295.

18. Byrd, A.K.; Raney, K.D. Protein displacement by an assembly of helicase molecules aligned along single-stranded DNA. *Nat. Struct. Mol. Biol.* **2004**, *11*, 531–538. https://doi.org/10.1038/nsmb774.

19. Delagoutte, E.; von Hippel, P.H. Helicase mechanisms and the coupling of helicases within macromolecular machines. Part II: Integration of helicases into cellular processes. *Q. Rev. Biophys.* **2003**, *36*, 1–69. https://doi.org/10.1017/s0033583502003864.

20. Sickmier, E.A.; Kreuzer, K.N.; White, S.W. The crystal structure of the UvsW helicase from bacteriophage T4. *Structure.* **2004**, *12*, 583–592. https://doi.org/10.1016/j.str.2004.02.016.

21. Ziebuhr, J. Molecular biology of severe acute respiratory syndrome coronavirus. *Curr. Opin. Microbiol.* **2004**, *7*, 412–419. https://doi.org/10.1016/j.mib.2004.06.007.

22. Kleymann, G.; Fischer, R.; Betz, U. A. K.; Hendrix, M.; Bender, W.; Schneider, U.; Handke, G.; Eckenberg, P.; Hewlett, G.; Pevzner, V. and et al. New helicase-primase

inhibitors as drug candidates for the treatment of herpes simplex disease. *Nat. Med.* **2002**, *8,* 392–398. https://doi.org/10.1038/nm0402-392.

23. Mirza, M. U.; Froeyen, M. Structural elucidation of SARS-CoV-2 vital proteins: Computational methods reveal potential drug candidates against main protease, Nsp12 polymerase and Nsp13 helicase. 2020, 2020030085, Preprints. doi: 10.20944/preprints202003.0085.v1 (accessed Apr 18, 2020.

24. Jia, Z.; Liming, Y.; Ren, Z.; Wu, L.; Wang, J.; Guo, J.; Zheng, L.; Ming, Z.; Zhang, L.; Lou, Z.; Rao, Z. Delicate structural coordination of the Severe Acute Respiratory Syndrome coronavirus Nsp13 upon ATP hydrolysis. *Nucleic Acids Res.* **2019**, *47*, 6538–6550. https://doi.org/10.1093/nar/gkz409.

25. Hao, W.; Wojdyla, J.A.; Zhao, R.I.; Han, R.; Das, R.; Zlatev, I.; Manoharan, M.; Wang, M.; Cui, S. Crystal structure of Middle East respiratory syndrome coronavirus helicase. *PLOS Pathog.* **2017**, *13,* e1006474. https://doi.org/10.1371/journal.ppat.1006474.

26. Briguglio, I.; Piras, S.; Corona, P.; Carta, A. Inhibition of RNA Helicases of ssRNA^{+} Virus Belonging to Flaviviridae, Coronaviridae and Picornaviridae Families. *Int. J. Med. Chem.* **2011**, *2011*, 213135. https://doi.org/10.1155/2011/213135.

27. Azmi, W.; Sani, R.K.; Banerjee, U.C. Biodegradation of triphenylmethane dyes. *Enzyme Microb. Technol.* **1998**, *22*, 185–191. https://doi.org/10.1016/s0141-0229(97)00159-2.

28. Le Guilloux, V.; Schmidtke, P.; Tuffery, P. Fpocket: An open source platform for ligand pocket detection. *BMC Bioinformatics.* **2009**, 10, 168. https://doi.org/10.1186/1471-2105-10-168.

29. Wu, C.; Liu, Y.; Yang, Y.; Zhang, P.; Zhong, W.; Wang, Y.; Wang, Q.; Xu, Y.; Li, M.; Li, X.; and et al. Analysis of therapeutic targets for SARS-CoV-2 and discovery of potential drugs by computational methods. *Acta Pharm. Sin. B.* **2020**, https://doi.org/https://doi.org/10.1016/j.apsb.2020.02.008.

30. Yu, M. S.; Lee, J.; Lee, J. M.; Kim, Y.; Chin, Y. W.; Jee, J. G.; Keum, Y. S.; Jeong, Y. J. Identification of myricetin and scutellarein as novel chemical inhibitors of the SARS coronavirus helicase, nsP13. *Bioorg. Med. Chem. Lett.* **2012**, *22*, 4049–4054. https://doi.org/10.1016/j.bmcl.2012.04.081.

31. Tanner, J. A.; Zheng, B. J.; Zhou, J.; Watt, R. M.; Jiang, J. Q.; Wong, K. L.; Lin, Y. P.; Lu, L. Y.; He, M. L.; Kung, H. F.; and et al. The adamantane-derived bananins are potent inhibitors of the helicase activities and replication of SARS coronavirus. *Chem. Biol.* **2005**, *12*, 303–311. https://doi.org/10.1016/j.chembiol.2005.01.006.

32. Lee J.; Cho, J.; Ahn, H.; Jung, W.; Jeong, Y. A Novel Chemical Compound for Inhibition of SARS Coronavirus Helicase. *J. Microbiol. Biotechnol.* **2017**, *27*, 2070–2073. https://doi.org/10.4014/jmb.1707.07073.

33. Cho, J.; Lee, J.; Ahn, H. Identification of a Novel Small Molecule Inhibitor Against SARS Coronavirus Helicase. *J. Microbiol. Biotechnol.* **2015**, *25*, 2007–2010. https://doi.org/10.4014/jmb.1507.07078.

34. Adedeji, A. O.; Singh, K.; Kassim, A.; Coleman, C. M.; Elliott, R.; Weiss, S. R.; Frieman, M. B.; Sarafianos, S. G. Evaluation of SSYA10-001 as a replication inhibitor of severe acute respiratory syndrome, mouse hepatitis, and Middle East respiratory

syndrome coronaviruses. *Antimicrob. Agents Chemother.* **2014**, *58*, 4894–4898. https://doi.org/10.1128/AAC.02994-14.

35. Sliwoski, G.; Kothiwale, S.; Meiler, J.; Lowe, E. W., Jr. Computational methods in drug discovery. *Pharmacol. Rev.* **2013**, *66*, 334–395. https://doi.org/10.1124/pr.112.007336.

36. Roy, A.; Kucukural, A.; Zhang, Y. I-TASSER: a unified platform for automated protein structure and function prediction. *Nat. Protoc.* **2010**, *5*, 725–738. https://doi.org/10.1038/nprot.2010.5.

37. Davis, I. W.; Leaver-Fay, A.; Chen, V. B.; Block, J. N.; Kapral, G. J.; Wang, X.; Murray, L. W.; Arendall, W. B.; Snoeyink, J., III.; Richardson, J. S.; Richardson, D.C. MolProbity: all-atom contacts and structure validation for proteins and nucleic acids. *Nucleic Acids Res.* **2007**, *35*, W375-83. https://doi.org/10.1093/nar/gkm216.

38. Kim, S.; Chen, J.; Cheng, T.; Gindulyte, A.; He, J.; He, S.; Li, Q.; Shoemaker, B. A.; Thiessen, P. A.; Yu, B.; Zaslavsky, L.; Zhang, J.; Bolton, E. E. PubChem 2019 update: improved access to chemical data. *Nucleic Acids Res.* **2019**, *47*, D1102–D1109. https://doi.org/10.1093/nar/gky1033.

39. Atatreh, N.; Al Rawashdah, S.; Al Neyadi, S. S.; Abuhamdah, S. M.; Ghattas, M.A. Discovery of new butyrylcholinesterase inhibitors via structure-based virtual screening. *J. Enzyme Inhib. Med. Chem.* **2019**, *34*, 1373–1379. https://doi.org/10.1080/14756366.2019.1644329.

40. Dallakyan, S.; Olson, A. J. Small-molecule library screening by docking with PyRx. Methods *Mol. Biol.* **2015**, *1263*, 243–250. https://doi.org/10.1007/978-1-4939-2269-7_19.

41. Trott, O.; Olson, A.J. AutoDock Vina: improving the speed and accuracy of docking with a new scoring function, efficient optimization, and multithreading. *J. Comput. Chem.* **2010**, *31*, 455–461. https://doi.org/10.1002/jcc.21334.

42. Pires, D. E. V.; Tom, L.; Blundell, D. B.; Ascher. pkCSM: Predicting Small-Molecule Pharmacokinetic and Toxicity Properties Using Graph-Based Signatures. *J. Med. Chem.* **2015**, *58*, 4066–4072. https://doi.org/10.1021/acs.jmedchem.5b00104.

43. Daina, A.; Olivier, M.; Vincent, Z. SwissADME: a free web tool to evaluate pharmacokinetics, drug-likeness and medicinal chemistry friendliness of small molecules. *Sci. Rep.* **2017**, *7*, 42717. https://doi.org/10.1038/srep42717.

44. Molinspiration. Calculation of molecular properties and bioactivity score. 2020. https://www.molinspiration.com/cgi-bin/properties.

45. DeLano, W. L. Pymol: An open-source molecular graphics tool. *CCP4 Newsl. Protein Crystallogr.* **2002**, *40*, 82–92.

46. Salentin, S.; Schreiber, S.; Haupt, V.J.; Adasme, M.F.; Schroeder, M. PLIP: fully automated protein-ligand interaction profiler. *Nucleic Acids Res.* **2015**, *43*, W443-7. https://doi.org/10.1093/nar/gkv315.

47. Le Guilloux, V.; Schmidtke, P.; Tuffery, P. Fpocket: An open source platform for ligand pocket detection. *BMC Bioinformatics.* **2009**, 10, 168. https://doi.org/10.1186/1471-2105-10-168.

48. Abraham, M.J.; Murtola, T.; Schulz, R.; Páll, S.; Smith, J.C.; Hess, B.; Lindahl, E. GROMACS: High performance molecular simulations through multi-level parallelism from laptops to supercomputers. *SoftwareX*. **2015**, *1–2*, 19–25. https://doi.org/https://doi.org/10.1016/j.softx.2015.06.001.

49. Dodda, L. S.; Cabeza de Vaca, I.; Tirado-Rives, J.; Jorgensen, W. L. LigParGen web server: an automatic OPLS-AA parameter generator for organic ligands. *Nucleic Acids Res.* **2017**, *45*, W331–W336. https://doi.org/10.1093/nar/gkx312.

50. Afgan, E.; Baker, D.; van den Beek, M.; Blankenberg, D.; Bouvier, D.; Cech, M.; Chilton, J.; Clements, D.; Coraor, N.; Eberhard, C.; Gruning, B.; Guerler, A.; Hillman-Jackson, J.; Von Kuster, G.; Rasche, E.; Soranzo, N.; Turaga, N.; Taylor, J.; Nekrutenko, A.; Goecks, J. The Galaxy platform for accessible, reproducible and collaborative biomedical analyses: 2016 update. *Nucleic Acids Res.* **2016**, *44*, W3–W10. https://doi.org/10.1093/nar/gkw343.

51. Gasteiger J.; Engel, T. *Chemoinformatics-A textbook;* Wiley-VCH: Germany, 2003.

52. Miller, M.A. Chemical database techniques in drug discovery. *Nat. Rev. Drug Discov.* **2002**, *1*, 220–227. https://doi.org/10.1038/nrd745.

53. Hopfinger, A. J.; Duca, J. S. Extraction of pharmacophore information from high-throughput screens. *Curr. Opin. Biotechnol.* 2000, *11*, 97–103. https://doi.org/10.1016/S0958-1669(99)00061-0.

54. Lipinski C. A.; Lombardo F.; Dominy B. W.; Feeney P. J. Experimental and computational approaches to estimate solubility and permeability in drug discovery and development settings. *Adv. Drug Deliv. Rev.* **2001**, *46*, 3–26. https://doi.org/10.1016/s0169-409x(00)00129-0.

55. Veber, D. F.; Johnson, S. R.; Cheng, H. Y.; Smith, B. R.; Ward, K. W.; Kopple, K. D. Molecular properties that influence the oral bioavailability of drug candidates. *J. Med. Chem.* **2002**, *45*, 2615–2623. https://doi.org/10.1021/jm020017n.

56. Ghose, A. K.; Viswanadhan, V. N.; Wendoloski, J. J. A knowledge-based approach in designing combinatorial or medicinal chemistry libraries for drug discovery. A qualitative and quantitative characterization of known drug databases. *J. Comb. Chem.* **1999**, *1*, 55–68. https://doi.org/10.1021/cc9800071.

57. Hitchcock, S. A.; Pennington, L. D.; Structure−Brain Exposure Relationships. *J. Med. Chem.* **2006**, *49*, 7559–7583. https://doi.org/10.1021/jm060642i.

58. Clemons, P.A.; Bodycombe, N.E.; Carrinski, H.A.; Wilson, J.A.; Shamji, A.F.; Wagner, B.K.; Koehler, A.N.; Schreiber, S.L. Small molecules of different origins have distinct distributions of structural complexity that correlate with protein-binding profiles. *Proc. Natl. Acad. Sci. U. S. A.* **2010**, *107*, 18787–18792. https://doi.org/10.1073/pnas.1012741107.

59. Capuzzi, S. J.; Muratov, E.N.; Tropsha, A. Phantom PAINS: Problems with the Utility of Alerts for Pan-Assay Interference Compounds. *J. Chem. Inf. Model.* **2017**, *57*, 417–427. https://doi.org/10.1021/acs.jcim.6b00465.

60. Khan, T.; Dixit, S.; Ahmad, R.; Raza, S.; Azad, I.; Joshi, S.; Khan, A. Molecular docking, PASS analysis, bioactivity score prediction, synthesis, characterization and biological activity evaluation of a functionalized 2-butanone thiosemicarbazone ligand and its complexes. *J. Chem. Biol.* **2017**, *10*, 91–104. https://doi.org/10.1007/s12154-017-0167-y.

61. Wilson, E.K. Picking the winners. *Chem. Eng. News*. **2002**, 35–39.

62. Baxter, A. D.; Lockey, P. M. 'Hit' to 'lead' and 'lead' to 'candidate' optimization using multi-parametric principles. *Drug Discov. World*. **2001**, *2*, 9-15.

63. Johnson-Davis, K. L.; Dasgupta, A. Chapter 11 - Special Issues in Therapeutic Drug Monitoring in Patients With Uremia, Liver Disease, and in Critically Ill Patients. In *Clinical Challenges in Therapeutic Drug Monitoring;* Clarke, W., Dasgupta, A., Eds.; Elsevier: San Diego, 2016; pp. 245–260. https://doi.org/https://doi.org/10.1016/B978-0-12-802025-8.00011-8.

64. Savjani, K. T.; Gajjar, A. J.; Savjani. K. J. Drug solubility: importance and enhancement techniques. *ISRN Pharm.* **2012**, *2012*, 195727. https://doi.org/10.5402/2012/195727.

65. Zhou, S.F. Drugs behave as substrates, inhibitors and inducers of human cytochrome P450 3A4. *Curr. Drug Metab.* **2008**, *9*, 310–322. https://doi.org/10.2174/138920008784220664.

66. Hacker, K.; Maas, R.; Kornhuber, J.; Fromm, M.F.; Zolk, O. Substrate-Dependent Inhibition of the Human Organic Cation Transporter OCT2: A Comparison of Metformin with Experimental Substrates. *PLoS One.* **2015,** *10,* e0136451. https://doi.org/10.1371/journal.pone.0136451.

67. Kenny, P.; Leitao, A.; Montanari, C. Ligand efficiency metrics considered harmful. *J. Comput. Aided. Mol. Des.* **2014**, *28*. https://doi.org/10.1007/s10822-014-9757-8.

68. Freire, E. A thermodynamic approach to the affinity optimization of drug candidates. *Chem. Biol. Drug Des.* **2009**, *74*, 468–472. https://doi.org/10.1111/j.1747-0285.2009.00880.x.

69. Jensen, J.H. Predicting accurate absolute binding energies in aqueous solution: thermodynamic considerations for electronic structure methods. *Phys. Chem. Chem. Phys.* **2015**, *17*, 12441–12451. https://doi.org/10.1039/C5CP00628G.

70. Natarajan, A.; Schwans, J.P.; Herschlag, D. Using unnatural amino acids to probe the energetics of oxyanion hole hydrogen bonds in the ketosteroid isomerase active site. *J. Am. Chem. Soc.* **2014**, *136*, 7643–7654. https://doi.org/10.1021/ja413174b.

71. Taylor, M. S.; Jacobsen, E. N. Asymmetric Catalysis by Chiral Hydrogen-Bond Donors. *Angew. Chemie Int. Ed.* **2006**, *45*, 1520–1543. https://doi.org/10.1002/anie.200503132.

72. Salentin, S.; Haupt, V. J.; Daminelli, S.; & Schroeder, M. Polypharmacology rescored: protein-ligand interaction profiles for remote binding site similarity assessment. *Prog. Biophys. Mol. Biol.* **2014**, *116*, 174–186. https://doi.org/10.1016/j.pbiomolbio.2014.05.006.

73. Sarkar, A.; Kellogg, G. E. Hydrophobicity-shake flasks, protein folding and drug discovery. *Curr. Top. Med. Chem.* **2010,** *10,* 67–83. https://doi.org/10.2174/156802610790232233.

74. Jeffrey, G.A. *An Introduction to Hydrogen Bonding* [Online]; Oxford University Press, 1997. https://books.google.com.ng/books?id=ZRAFifo37QsC.

75. Desiraju, G.; Steiner, T. The Weak Hydrogen Bond. In *Structural Chemistry and Biology*; Oxford University Press: Oxford, 2001. https://doi.org/10.1093/acprof:oso/9780198509707.001.0001.

76. Kumar, S.; Nussinov, R. Close-range electrostatic interactions in proteins. *Chembiochem.* **2002**, *3*, 604–617. https://doi.org/10.1002/1439-7633(20020703)3:7<604::AID-CBIC604>3.0.CO;2-X.

77. Kenny, P.W. The nature of ligand efficiency. *J. Cheminform.* **2019**, *11*, 8. https://doi.org/10.1186/s13321-019-0330-2.

78. Kufareva, I.; Abagyan, R. Methods of protein structure comparison. *Methods Mol. Biol.* **2012**, *857*, 231–257. https://doi.org/10.1007/978-1-61779-588-6_10.

79. Stockner, T.; Vogel, H. J.; Peter Tieleman, D. A salt-bridge motif involved in ligand binding and large-scale domain motions of the maltose-binding protein. *Biophys. J.* **2005**, *89*, 3362–3371. https://doi.org/10.1529/biophysj.105.069443.

80. Krzysztof, K.; Gouri, S.J.; Ron, E. Kinetics of helix unfolding: molecular dynamics simulations with milestoning. *J. Phys. Chem. A.* **2009**, *113*, 7461–7473. https://doi.org/10.1021/jp900407w.

81. Rajesh, D. Re: What is the importance of the RMSD value in molecular docking? 2015. https://www.researchgate.net/post/What_is_the_importance_of_the_RMSD_value_in_molecular_docking/556301ab614325252e8b45b2/citation/download. (accessed May 28, 2020).

82. Gürsoy, O.; Smieško, M. Searching for bioactive conformations of drug-like ligands with current force fields: how good are we?. *J. Cheminform.* **2017**, *9*, 29. https://doi.org/10.1186/s13321-017-0216-0.

83. Fuglebakk, E.; Echave, J.; Reuter, N. Measuring and comparing structural fluctuation patterns in large protein datasets. *Bioinformatics.* **2012**, *28*, 2431–2440. https://doi.org/10.1093/bioinformatics/bts445.

84. David, C.C.; Jacobs, D.J. Principal component analysis: a method for determining the essential dynamics of proteins. *Methods Mol. Biol.* **2014**, *1084*, 193–226. https://doi.org/10.1007/978-1-62703-658-0_11.

85. Sawle, L.; Ghosh, K. Convergence of Molecular Dynamics Simulation of Protein Native States: Feasibility vs Self-Consistency Dilemma. *J. Chem. Theory Comput.* **2016**, *12*, 861–869. https://doi.org/10.1021/acs.jctc.5b00999.

86. Upadhyay, S.K. Dynamics of Gal80p in the Gal80p–Gal3p complex differ significantly from the dynamics in the Gal80p–Gal1p complex: implications for the higher specificity of Gal3p. *Mol. Biosyst.* **2014**, *10*, 3120–3129. https://doi.org/10.1039/C4MB00371C.

87. Kasahara, K., Fukuda, I., Nakamura, H. A Novel Approach of Dynamic Cross Correlation Analysis on Molecular Dynamics Simulations and Its Application to Ets1

Dimer–DNA Complex. *PLoS One.* **2014**, 9, e112419. https://doi.org/10.1371/journal.pone.0112419.

88. Vidhyasekaran, P. Gibberellin Signaling in Plant Innate Immunity. In *Plant Hormone Signalling. Systems in Plant Innate Immunity*, Springer: Netherlands, 2015; pp 383–401.

89. Smith, V.A. Gibberellin A1 Biosynthesis in Pisum sativum L. : II. Biological and Biochemical Consequences of the le Mutation, *Plant Physiol.* **1992**, *99*, 372–377. https://doi.org/10.1104/pp.99.2.372.

90. Bailiss, K.W. The relationship of gibberellin content to cucumber mosaic virus infection of cucumber. *Physiol. Plant Pathol.* **1974**, *4*, 73–79. https://doi.org/https://doi.org/10.1016/0048-4059(74)90046-0.

91. Rowaiye, A. B.; Olubiyi, J.; Bur, D.; Uzochukwu, I. C.; Akpa, A.; & Esimone, C. O. *In silico* screening and molecular dynamic simulation studies of potential small molecule immunomodulators of the kir2ds2 receptor. 2020, 2020.05.10.087148. BioRxiv. https://doi.org/10.1101/2020.05.10.087148.

92. De Bruyne, L.; Höfte, M.; De Vleesschauwer, D. Connecting growth and defense: the emerging roles of brassinosteroids and gibberellins in plant innate immunity. *Mol. Plant.* **2014**, *7*, 943–959. https://doi.org/10.1093/mp/ssu050.